frontiers | Frontiers in Marine Science

TYPE Original Research
PUBLISHED 08 November 2024
DOI 10.3389/fmars.2024.1490890

OPEN ACCESS

EDITED BY
Kumbukani Mzengereza,
Mzuzu University, Malawi

REVIEWED BY
Dongdong Shao,
Beijing Normal University, China
Simone Bonamano,
University of Tuscia, Italy

*CORRESPONDENCE
Manel Grifoll
manel.grifoll@upc.edu

RECEIVED 03 September 2024
ACCEPTED 17 October 2024
PUBLISHED 08 November 2024

CITATION
Grifoll M, Cuthbertson A, Peñas-Torramilans R and Davies P (2024) Experimental investigation of surface buoyant jet interactions with grid obstructions: implications for aquaculture.
*Front. Mar. Sci.* 11:1490890.
doi: 10.3389/fmars.2024.1490890

# Experimental investigation of surface buoyant jet interactions with grid obstructions: implications for aquaculture

Manel Grifoll[1,2]*, Alan Cuthbertson[2], Raquel Peñas-Torramilans[1] and Peter Davies[2]

[1]Laboratori d'Enginyeria Marítima, Universitat Politècnica de Catalunya (UPC-BarcelonaTech), Barcelona, Spain, [2]School of Science and Engineering (Civil Engineering), University of Dundee, Dundee, Scotland, United Kingdom

Freshwater inputs originating from terrestrial streams and gullies that discharge into quiescent, semi-enclosed coastal regions (such as estuaries, tidal inlets or lagoons), typically provide point sources of nutrients (e.g. nitrates, phosphates) and/or contaminants (e.g. pesticides, pathogens) that may have a deleterious impact on water quality. Many of these sheltered coastal regions also increasingly support aquaculture operations (e.g. finfish, shellfish, or seaweed farms), which can therefore be directly impacted by nutrient and contaminant inputs. Dynamically, these terrestrial freshwater inflows behave as surface buoyant jets or plumes within the coastal saline or brackish receiving waters, due to the salinity-induced density gradients. As such, the presence of infrastructure associated with aquaculture operations in sheltered coastal waters can provide obstruction to the propagation characteristics and residence times for these surface freshwater flows. Consequently, an improved physical understanding of the flow-structure interaction is clearly crucial to assessing the potential contamination risk of aquaculture products. The aim of the current study is therefore to explore, through scaled laboratory experiments within a channel-basin facility, the impact of physical obstruction induced by a vertical grid structure on the flow evolution of a 2D – 3D expanding, surface buoyant jet. Two grid obstructions with different solidity ratios are tested, along with surface gravity currents of different density excesses and freshwater inflows to infer the influence of different parametric conditions on the propagation, blockage and mixing characteristics of the surface current in the vicinity of the grid obstruction. Measurements of the velocity structure and thickness of the expanding surface plume are obtained by ultrasonic velocity profilers, while the density excess in the evolving plume is measured by micro-conductivity probes. Dye visualization results also show that, in the presence of the grid obstruction, the generation of shear-induced billows at the lower interface of the expanding surface current is largely blocked and a local deepening of the fresh-salt water interface in the immediate vicinity of the grid obstruction is observed. In this sense, the obstruction imposed by aquaculture infrastructure in coastal domains can have a considerable influence of the local turbulent mixing and vertical transfer of substances (e.g. nutrients and contaminants), but is likely to have relatively minimal impact in the final dispersion of the surface plume.

KEYWORDS

**surface buoyant jet, interface instability, laboratory experiments, mussels rafts, oyster rafts**

## 1 Introduction

Freshwater inputs from terrestrial sources entering sheltered coastal waters can form surface buoyant jets due to the density difference between the intruding freshwater and the saline or brackish waters present in the receiving aquatic environment. This inflowing freshwater jet can contain nutrients, such as nitrates or phosphates, and/or other harmful contaminants, such as pesticides and pathogens, that can impact negatively on water quality, the coastal ecosystem and the potential for aquaculture development (Ramón et al., 2007; García-Altares et al., 2016). In particular, while the presence of low nutrient concentrations can promote the growth of phytoplankton and other organisms, higher nutrient concentrations may lead to eutrophication in the receiving water body, with associated oxygen depletion and algal blooms. These nutrient and contaminant inputs can be particularly problematic following significant rainfall events, where large volumes of highly contaminated freshwater can contribute to significant detrimental impacts on water quality within these near-shore saline or brackish water environments (León et al., 2017; Cerralbo et al., 2019; Balsells F-Pedrera et al., 2021). Other chemical and/or biological contaminants (and, in some cases, sediment) contained within rainfall runoff can also significantly impact on water quality and pose potential harm to aquatic life and human health if they reach sufficiently high concentrations. In this sense, sheltered coastal water bodies can become heavily contaminated by deficient water quality from terrestrial freshwater discharges (León et al., 2017; Erena et al., 2019), meaning that an enhanced understanding of the dynamics of surface plumes is therefore crucial for managing the health of coastal ecosystems and protecting public health.

Many sheltered coastal regions increasingly support infrastructure associated with near-shore aquaculture operations (e.g. finfish, shellfish, or seaweed farms) or, more locally, trash traps in adjacent gullies and channels designed to prevent plastic materials discharging into the coastal waters (Zayed et al., 2018). The interaction of surface jets with this infrastructure can provide obstructions to the surface freshwater flow propagation, impacting on the flushing capacity of coastal embayments (Shao et al., 2021; Lin et al., 2019) and, hence, increasing the residence time of contaminants. Relevant previous studies have been found to investigate the hydrodynamic impacts of specific types of aquaculture installations (e.g. oyster and mussels farms) often in the pursuit of more effective infrastructure configurations to improve water exchange, amongst other properties (Fredriksson et al., 2010; Gaurier et al., 2011; Landmann et al., 2021). Other experimental and numerical studies have focused more on specific elements of caged aquaculture infrastructure, such as flexible and rigid planar net panels (Shao et al., 2021; Zeng et al., 2022; Yang et al., 2022; González-Ávalos et al., 2024), to assess their impact on turbulent flow characteristics in the immediate vicinity of the net panel. In most cases, these studies have identified a non-negligible increase in the drag coefficients due to the local obstruction effect that the presence of solid bodies has on flow perturbations and turbulence properties close to the infrastructure. However, the equivalent impact that aquaculture infrastructure has on surface buoyant discharge flows (with the potential differences in temperature/salinity from the receiving waters) has not yet been investigated. As such, better physical understanding of this buoyant flow-structure interaction is clearly crucial to assessing the blockage and retention time of contaminated surface jets, resulting in potential contamination risk to the aquaculture products and a detrimental impact on the coastal ecosystem.

A number of numerical model studies have been conducted to investigate surface water circulation in sheltered micro-tidal estuaries, bays and lagoons, and have demonstrated good agreement with *in-situ* water current and stratification measurements (e.g. Cerralbo et al., 2019; Balsells F-Pedrera et al., 2020; Umgiesser et al., 2014; Bonamano et al., 2021). In some of these locations (for instance, Alfacs and Fangar bays in the Ebro Delta, NW Mediterranean Sea), a significant percentage of the enclosed coastal water surface area is covered by aquaculture infrastructure, which acts as an obstruction to the surface flow, the effects of which have not been included in a systematic manner within these numerical model investigations. Physical obstructions within these settings may not only be due to aquaculture operations, but may also arise from the impact of jetties and marinas that can act as obstructions to wastewater outflow systems. In this regard, Huguet et al. (2020) investigated the impact from marina structures on tide- and wind-driven hydrodynamics, providing numerical predictions for frictional effects of the obstructions on circulation patterns. In contrast to their study in tidally-active regions, surface flow-infrastructure interactions in enclosed, micro-tidal coastal regions, with the presence of vertical gradients in both the velocity and density profiles throughout the water depth (e.g. Balsells F-Pedrera et al., 2020), presents clear differences in the underlying hydrodynamics. Such a finding justifies the current investigation of expanding surface buoyant plume interactions with grid obstructions. The results from the idealized laboratory experiments presented herein thus add to the existing knowledge from these numerical modelling studies, particularly in providing more accurate local representations of the interaction between expanding surface buoyant jets and aquaculture infrastructure. In this regard, explicit parametrization in these numerical models would be valuable to capture the effects of the grid obstructions on partial flow blockage, local thickening with associated vertical mixing of the surface layer in the immediate vicinity of the obstruction and wider stabilization of the stratified flow.

The work presented in this paper is based on scaled laboratory modelling of surface buoyant jet interactions with grid obstructions. The main motivation of this study is to better understand the transport and mixing mechanisms of freshwater discharges into a quiescent saline water body in the presence of a specific flow obstruction that is used to provide an idealized representation of the infrastructure associated with aquaculture operations (e.g. finfish, shellfish, or seaweed farms). The aim of the study is therefore to determine the parametric dependence of the flow evolution and mixing characteristics of an incident surface buoyant jet on the obstruction geometry (i.e. grid solidity ratio of an idealized vertical grid structure). The paper is organized as follows: after the Introduction (Section 1), the Physical System, including descriptions of the laboratory facility, the experimental set-up and instrumentation, are presented in Section 2. Section 3 includes the main experimental results and provides a qualitative comparison with a real test case in a micro-tidal environment (e.g. Fangar bay in NW Mediterranean Sea). The key findings from the experimental results are then discussed in Section 4. Finally, the paper closes with the main conclusions (Section 5).

## 2 The physical system

A schematic representation of the problem under investigation is presented in Figure 1, with the nomenclature table of abbreviations and variables also provided in Table 1. The initial, undisturbed system is one in which the saline water of density $\rho_2$ fills a channel $C$ and basin $B$ facility to a maximum depth $H_b$. The channel $C$ of width $B_c$ has an inclined sloping bottom of constant slope $\alpha$. A freshwater flow of density $\rho_1$ and discharge rate $Q_1$ is introduced at the top of the sloping channel via an inlet manifold $M$ located at a distance $L_c$ from the channel exit. This freshwater flow reaches a porous reticulated foam layer $F$ (located at $L_f$ from the manifold) in

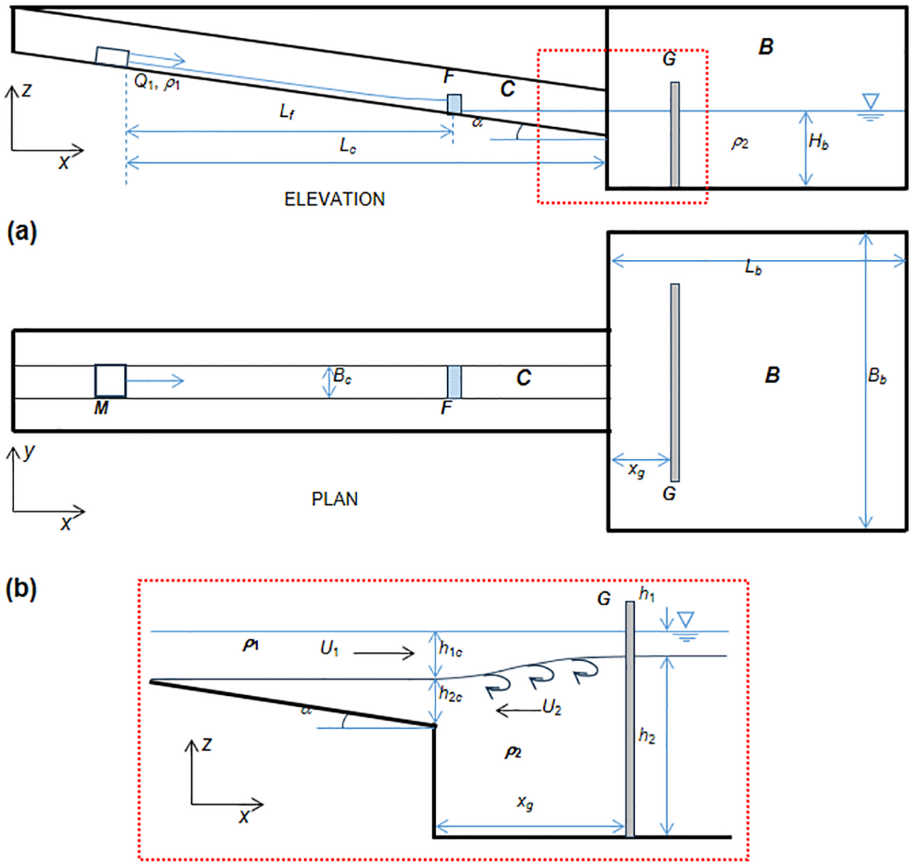

FIGURE 1
Schematic diagram of **(A)** the experimental model facility and **(B)** the physical system under investigation.

TABLE 1 Summary of main nomenclature of symbols and variables used in the analysis.

| Experimental set up | | | Physical variables | | |
|---|---|---|---|---|---|
| $\alpha$ | Channel slope | [-] | $\delta$ | Interface layer thickness | [L] |
| $\varnothing$ | Solidity | [-] | $\overline{\Delta\rho}$ | Averaged density excess | $[M{\cdot}L^{-3}]$ |
| $B_b$ | Wider basin width | [L] | $\Delta\rho$ | Density excess | $[M{\cdot}L^{-3}]$ |
| $B_c$ | Channel width | [L] | $\rho$ | Density | $[M{\cdot}L^{-3}]$ |
| $D$ | Width of solid bars | [L] | $\rho'$ | Density fluctuations | $[M{\cdot}L^{-3}]$ |
| $H_b$ | Maximum depth | [L] | $\rho_1$ | Freshwater flow density | $[M{\cdot}L^{-3}]$ |
| $H_c$ | Depth at channel exit | [L] | $\rho_2$ | Saline water density | $[M{\cdot}L^{-3}]$ |
| $L$ | Length of the channel | [L] | $\rho_a$ | Ambient density | $[M{\cdot}L^{-3}]$ |
| $L_b$ | Length of the basin | [L] | $\rho_{c2}$ | Surface density at probe C2 | $[M{\cdot}L^{-3}]$ |
| $L_c$ | Distance between manifold and channel exit | [L] | $\bar{\rho}$ | Mean surface layer density | $[M{\cdot}L^{-3}]$ |
| $L_f$ | Distance between manifold and foam | [L] | $Fr_d$ | Densimetric Froude number | [-] |
| $s/d$ | Space-to-bar thickness ratio | [-] | $g'$ | Reduced gravity acceleration | $[L{\cdot}T^{-2}]$ |
| $s$ | Gap width between solid bars | [L] | $h_1$ | Upper layer thickness | [L] |
| $x_g$ | Obstruction downstream distance | [L] | $h_{1C}$ | Freshwater thickness at layer exit | [L] |
| | | | $l_M$ | Jet/plume transition length scale | [L] |
| | | | $Re$ | Reynolds number | [-] |
| | | | $Ri$ | Richardson number | [-] |
| | | | $Ri_g$ | Gradient Richardson number | [-] |
| | | | $t$ | Head plume travel time | [T] |
| | | | $Q_1$ | Discharge rate | $[L^3{\cdot}T^{-1}]$ |
| | | | $\Delta u$ | Velocity difference | $[L{\cdot}T^{-1}]$ |
| | | | $\bar{u}$ | Mean velocity | $[L{\cdot}T^{-1}]$ |
| | | | $\bar{u}_1$ | Mean surface layer velocity | $[L{\cdot}T^{-1}]$ |
| | | | $u_{max}$ | Maximum velocity | $[L{\cdot}T^{-1}]$ |
| | | | $U_1$ | Surface layer velocity | $[L{\cdot}T^{-1}]$ |
| | | | $U_2$ | Lower layer velocity | $[L{\cdot}T^{-1}]$ |
| | | | $x_f$ | Frontal position | [L] |

the channel at the free surface of the saline water volume, through which it diffuses and flows out as a surface gravity current. On reaching the end of the confined channel *C*, the surface gravity current loses lateral confinement and expands into the wider basin (of width $B_b$) as a surface plume. At a downstream distance $x_g$ from the channel exit, a vertical grid obstruction *G* of solidity $\phi$ [i.e. related to the space-to-bar thickness ratio $s/d$ of the obstruction, such that $\phi = d/(s + d)$] is placed perpendicular to the main flow direction, where it interacts with the expanding plume. The main purpose of the present laboratory model study is to monitor and quantify the details of the outflowing surface layer of velocity $U_1$ and thickness $h_1$ on exit from channel *C* and its encounter with the vertical grid structure in the basin *B*. Different parametric conditions are introduced by changes to (i) the density excess $\Delta\rho = \rho_2 - \rho_1$ between the fresh and saline water masses; (ii) the freshwater inflow rate $Q_1$; and (iii) the solidity $\phi$ of the vertical grid obstruction. Figure 1 shows the Cartesian co-ordinate system $(x, y, z)$ within which the spatial and temporal development of the surface flow is described; the flow is assumed to be two-dimensional within channel *C*, with a loss of confinement and lateral expansion in the cross-channel ($y$) direction on entering basin *B*. The $z$ axis is taken to be anti-parallel to the gravitational acceleration vector $\mathbf{g} = (0, 0, -g)$.

## 2.1 Experimental facility and set-up

The scaled laboratory experiments were conducted in an acrylic-walled channel-basin facility. This consists of a narrow, sloping channel section of overall length $L = 4.0$ m, width $B_c = 0.1$ *m* and bottom slope $\alpha = 3°$, exiting into a large, horizontal-bottomed basin with plan form dimensions $L_b = B_b = 2.0$ m (Figure 2A). A water volume of density $\rho_2$ varying between prescribed values of 1000, 1010 and 1020 kg.m$^{-3}$ respectively filled the basin to a total depth $H_b = 0.225$ m (see Figure 1), with the equivalent depth at the channel exit $H_c = 0.115$ m (note: $H_c = h_{1c} + h_{2c}$ in Figure 1B). Freshwater ($\rho_1 = 1000$ kg.m$^{-3}$) from a pumped source tank was introduced to the upper sloping channel through the inlet manifold ($L_c = 3.16$ m) with values of the initial volume flux $Q_1$ ranging from 0.24 to 0.49 l.s$^{-1}$. This freshwater flow down the channel slope was damped by the reticulated foam block (to dissipate initial momentum; $L_f = 2.35$ m) before entering the channel-basin water volume as a surface gravity current (for runs with an initial density difference $\Delta\rho = \rho_2 - \rho_1$ between the channel and basin waters). On exit from the confined channel, the gravity current propagated into the basin as an expanding, three-dimensional surface buoyant plume. As the channel-basin facility is fully enclosed, the additional freshwater input increased the overall depth within the basin during an individual run. However, over the typical freshwater inflow duration of 40 s, this corresponded to an increase in water level within the facility of $O(10^{-4}$ m) and, hence, was considered negligible. Furthermore, the durations of each freshwater inflow were limited to ensure that reflections and recirculation from the expanding gravity current within the basin did not affect the experimental measurements.

Experimental observations of the spatial and temporal evolution of the surface gravity current between the confined channel and unconfined basin were obtained through a combination of qualitative dye tests and quantitative time series

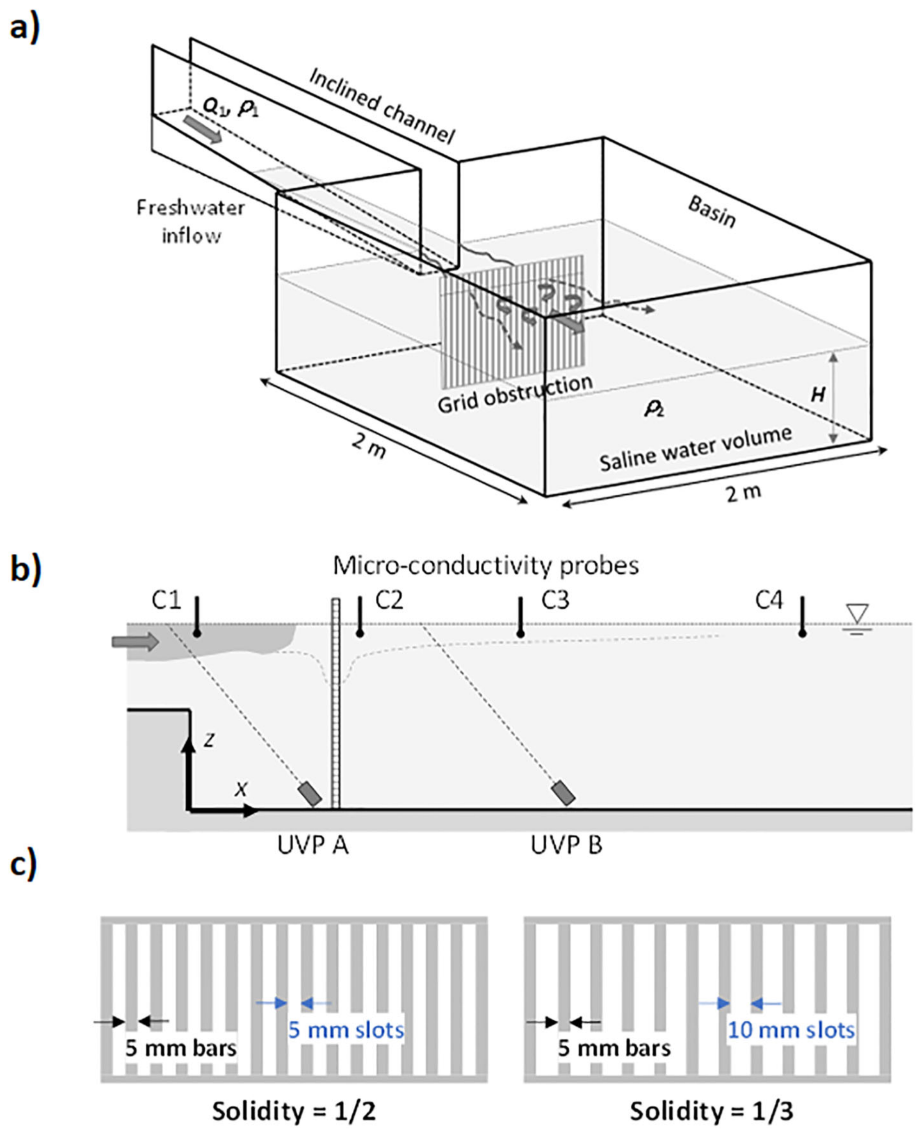

FIGURE 2
**(A)** 3D schematic representation of the experimental set-up including the freshwater discharge channel and a sketch of the grid obstruction. **(B)** Centreline channel view with the location of the instrumentation (i.e. micro-conductivity probes C1 – C4 and UVP transducers UVP A and UVP B). (Note: The downstream distances from the channel exit to probes C1 to C4 are 0.04 m, 0.30 m, 0.56 m and 0.82 m, respectively). **(C)** Details of the geometry of the vertical grid obstructions with solidity = 1/2 (i.e. s/d = 1.0) and 1/3 (i.e. s/d = 2.0) (note: overall grid length = 1.0 m and height = 0.25 m).

velocity profile and near-surface density measurements at a number of centreline positions, both at the channel exit and downstream into the basin (see Figure 2B). For a number of experimental runs, a 1 m-long rectangular grid obstruction was mounted transversely across the basin (in the *y-z* plane) at a distance $x_g$ = 0.25 m downstream from the channel exit. Two grid obstructions were tested, with solidity values of $\phi$ = 1/2 and 1/3, respectively and typical of field conditions. In both cases, the widths of the solid bars in the vertical grid were kept constant at $d$ = 0.5 cm wide, with the solidity differing as a result of the gap width between these solid bars (i.e. $s$ = 0.5 cm and 1.0 cm, respectively, such that $s/d$ = 1.0 and 2.0) (see Figure 2C).

Partially obstructed flow simulations in the presence of grid obstructions were compared directly with equivalent benchmark runs with no obstruction in place within the basin (i.e. $\phi$ = 0, $s/d$ = infin;). In both cases, velocity and density measurements were taken at the fixed locations upstream and downstream of the grid obstruction (see Figure 2B). The 1 m overall length of the grid obstructions, and its positioning relative to the channel exit, avoided any lateral bypassing of expanding freshwater surface plume around the lateral extent of the obstruction, with the full obstructed surface gravity current passing through the grid obstruction. A summary of the different parametric conditions tested within the experimental runs are summarized in Table 2.

Within the current experimental configuration, time series velocity profile measurements were obtained by two MetFlow UVP transducers positioned 0.11 m above the basin bed level and angled 45° relative to horizontal basin bottom, pointing upstream (i.e. UVP A and UVP B at x = 0.23 m and 0.75 m respectivelly Figure 2B). This UVP technique measures flow velocities along the entire transducer beam axis (shown as dashed lines in Figure 2B), which are then converted into a bed parallel velocity components. This measurement technique is known to be satisfactory for shallow flows, where vertical velocity components are negligible compared to the horizontal velocity components (e.g. Duma et al., 2014; Eggenhuisen et al., 2020; Wilkin et al., 2023). It also has the advantage of providing a full velocity profile through the water depth, rather than a single point timeseries measurements provided by other similar acoustic techniques, such as Acoustic Doppler Velocimeters (ADV). In each experimental run, time series measurements of surface velocity profiles were therefore measured at the channel exit (i.e. $x$ = 0 m) and $x$ = 0.5 m downstream of the channel exit using the UVP system. Time-averaged velocity profiles were then calculated for the main body of the current (after the initial passage of the current head), which are associated with quasi-steady freshwater inflow conditions.

Equivalent time-series density measurements were obtained using four micro-conductivity probes (Carminati and Luzzatto-Fegiz, 2017), positioned along a longitudinal channel-basin centreline transect at distances $x$ of 0.03 m, 0.27 m, 0.53 m and 0.79 m downstream of the channel exit. The measurement tip of the micro-conductivity probes were located 10 mm below the free water surface in order to measure the evolving surface freshwater plume. Each micro-conductivity probe was carefully calibrated against specific fresh, brackish and saline water solutions of known densities to enable direct conversion of micro-conductivity measurements to equivalent density values.

## 2.2 Scaling considerations

Important length scales to describe the near-field dynamics of surface buoyant jets and plumes discharging into initially-unstratified receiving waters can be defined in terms of the source values of discharge volume flux $Q_1$, the kinematic momentum flux $M_1$ and the kinematic buoyancy flux $B_1$ (e.g. Jirka et al., 1996). In the current experimental set-up, these fluxes can be defined at the channel exit (according to Figure 1B) as follows:

$$Q_1 = U_1 h_{1c} B_c \tag{1}$$

$$M_1 = Q_1 \,.\, U_1 = h_{1c} B_c U_1^2 \tag{2}$$

$$B_1 = g' \,.\, Q_1 = g' U_1 h_{1c} B_c \tag{3}$$

where $g' = g(\Delta\rho/\rho_1)$ is the reduced gravitational acceleration, and $U_1$ is the average velocity in the outflowing surface layer at the channel exit, estimated as:

$$U_1 = \frac{1}{h_{1c}} \int_{z=H_b-h_{1c}}^{z=H_b} u(z)dz \tag{4}$$

In terms of estimating the surface plume thickness $h_{1c}$ at the channel exit from the appropriate velocity profile measurements (i.e. UVP A, Figure 2B), this is taken as the depth from free surface to the elevation where the current velocity is equal to $u_{\max}/2$ (Gray et al., 2006), where $u_{\max}$ is the maximum, steady-state surface velocity measured in the outflowing surface layer obtained from the UVP A profiles. A characteristic length scale $l_M$ associated with

TABLE 2 Summary of main experimental variables and derived non-dimensional parameters.

| Run | $\Delta\rho$ (kg.m$^{-3}$) | $Q_1$ (l.s$^{-1}$) | $U_1$ (m.s$^{-1}$) (Equation 4) | $g'$ (m.s$^{-2}$) | Grid Solidity $\phi$ | $s/d$ | $l_M$ (m) (Equation 5) | $Fr_d$ (Equation 6) | $Re$ (Equation 9) |
|---|---|---|---|---|---|---|---|---|---|
| R1 | 0 | 0.489 | 0.0224 | 0.0 | 0, 1/3, 1/2 | ∞, 2, 1 | – | – | 8112 |
| R2 | 10 | 0.489 | 0.0468 | 0.098 | 0, 1/3, 1/2 | ∞, 2, 1 | 0.035 | 0.87 | 6336 |
| R3 | 20 | 0.489 | 0.0572 | 0.196 | 0, 1/3, 1/2 | ∞, 2, 1 | 0.029 | 0.80 | 7337 |
| R4 | 0 | 0.244 | 0.0198 | 0.0 | 0, 1/3, 1/2 | ∞, 2, 1 | – | – | 3162 |
| R5 | 20 | 0.244 | 0.0511 | 0.196 | 0, 1/3, 1/2 | ∞, 2, 1 | 0.026 | 0.71 | 5682 |

the transition between momentum-dominated (i.e. jet-like) behavior and buoyancy-dominated (i.e. plume-like) behavior of a surface buoyant jet discharging into an unstratified receiving water (Jirka et al., 1996), can be defined as follows:

$$l_M = M_1^{3/4} / B_1^{1/2} \tag{5}$$

This jet/plume transition length scale $l_M$ can be compared directly with a suitable geometrical length scale from the current experimental configuration (e.g. channel width $B_c$ or distance from channel exit to the grid obstruction $x_g$). The densimetric Froude number $Fr_d$ has often been used to describe the source conditions for buoyant jets and plumes, including surface flows (e.g. Fischer et al., 1979). Within the specific experimental configuration under investigation, this can be defined as follows, and related to the jet/plume transition length scale $l_M$ such that.

$$Fr_d = \frac{U_1}{(g' h_{1c})^{1/2}} = \left(\frac{l_M}{h_{1c}}\right)\left(\frac{h_{1c}}{B_c}\right)^{1/4} = \frac{l_M}{(B_c h_{1c}^3)^{1/4}} \tag{6}$$

Similarly, a local Richardson number $Ri$, based on bulk flow properties across the shear layer separating the buoyant surface outflow with the underlying water column, can be defined (e.g. De Falco et al., 2021), such that.

$$Ri = \frac{g' \delta}{\Delta u^2} \tag{7}$$

Where $g'$ is the local reduced gravitational acceleration and $\delta$ is the shear mixing layer thickness, defined as follows (Zhu and Lawrence, 2001):

$$\delta = \frac{\Delta u}{(du/dz)_{max}} \tag{8}$$

and $\Delta u = u_{1,max} - u_{2,min}$ is the local velocity difference between the surface layer and underlying ambient fluid. Finally, the flow Reynolds number for the outflowing surface flow is given by.

$$Re = \frac{4 U_1 h_{1c}}{\nu} \tag{9}$$

Indicative values for these non-dimensional parameters at the channel exit (see Tables 2, 3) suggest that the outflowing buoyant surface flows are subcritical (i.e. $Fr_d < 1$) and turbulent (i.e. $Re >$ 2,500). The local Richardson number $Ri$ values (i.e. $Ri > 0.25$) also indicate that the surface outflowing layer is generally stable with some degree of mixing observed at the lower interface with the ambient water (see Section 3.1). Finally, the calculated jet/plume transition length scale $l_M$ indicates that the expanding surface flow behaves as a buoyancy-dominated surface jet before it interacts with the vertical grid obstruction (i.e. $l_M / x_g \ll 1$), with the momentum-dominated (jet-like) conditions restricted to immediately downstream of the channel exit.

# 3 Experimental results

## 3.1 Qualitative observations (dye tests)

Dye tracing experimental runs were conducted to observe the evolving structure of the surface gravity current as it exits the channel

TABLE 3 Estimation of the bulk Richardson number $Ri$ [Equation 11] based on the maximum surface flow velocity $U_{1,max}$ (measured at UVP A and UVP B); the local reduced gravitational acceleration (based on local time-averaged density excess $\overline{\Delta\rho}$ calculated at probes C1 and C2); the maximum velocity gradient $(du/dz)_{max}$ in the time-averaged velocity profile (at UVP A and UVP B); and calculated shear layer thickness $\delta$ [Equation 8].

| | | UVP A | UVP B | Probe C1 | | Probe C2 | |
|---|---|---|---|---|---|---|---|
| Run No. | Grid $\phi$; s/d | $U_{1,max}$ (m.s$^{-1}$) | $U_{1,max}$ (m.s$^{-1}$) | $\overline{\Delta\rho}$ (kg.m$^{-3}$) | $g'$ (m.s$^{-2}$) | $\overline{\Delta\rho}$ (kg.m$^{-3}$) | $g'$ (m.s$^{-2}$) |
| R2 | 0; ∞ | 0.055 | 0.030 | 9.5 | 0.093 | 5.5 | 0.054 |
| R2 | 1/3; 2 | 0.058 | 0.025 | 9.5 | 0.093 | 7.0 | 0.069 |
| R2 | 1/2; 1 | 0.059 | 0.023 | 9.5 | 0.093 | 7.5 | 0.074 |
| R3 | 0; ∞ | 0.071 | 0.047 | 19.0 | 0.186 | 10.0 | 0.098 |
| R3 | 1/3; 2 | 0.071 | 0.038 | 19.0 | 0.186 | 13.0 | 0.128 |
| R3 | 1/2; 1 | 0.072 | 0.037 | 19.0 | 0.186 | 15.0 | 0.147 |
| | | UVP A | UVP B | UVP A | UVP B | UVP A | UVP B |
| | $\phi$; s/d | $(du/dz)_{max}$ | $(du/dz)_{max}$ | $\delta$ (m) | $\delta$ (m) | $Ri$ | $Ri$ |
| R2 | 0; ∞ | 2.192 | 1.505 | 0.025 | 0.020 | 0.78 | 1.21 |
| R2 | 1/3; 2 | 2.250 | 1.600 | 0.026 | 0.015 | 0.72 | 1.73 |
| R2 | 1/2; 1 | 2.519 | 1.855 | 0.023 | 0.012 | 0.63 | 1.75 |
| R3 | 0; ∞ | 5.000 | 1.145 | 0.014 | 0.041 | 0.53 | 1.82 |
| R3 | 1/3; 2 | 3.567 | 2.105 | 0.020 | 0.018 | 0.74 | 1.61 |
| R3 | 1/2; 1 | 3.442 | 1.920 | 0.021 | 0.019 | 0.75 | 2.07 |

into the basin. These tests also provided an initial indication of the influence of the vertical grid obstruction on the behavior of the surface buoyant jet. Figure 3 shows a time sequence of dye images in which the unobstructed frontal propagation of the current head into the basin is clearly defined (Run 5: $\Delta\rho$ = 20 kg.m$^{-3}$; $Q_1$ = 0.244 l.s$^{-1}$, Table 2). Once the quasi-steady surface outflow layer has been established (Figure 3H), it is interesting to note that the current thickness $h_1$ diminishes immediately downstream from the channel exit (i.e. where $h_1 = h_{1c}$) as the surface current loses confinement. Further into the basin, there is also visual evidence of the formation of billows associated with Kelvin-Helmholtz instability at the lower interface of the expanding current with the underlying ambient fluid. The surface layer continues to diminish in thickness with increasing downstream distance due to the continued lateral spread of the current.

Figure 4 shows a similar time sequence of dye tracing images for a surface outflow interacting with a vertical grid obstruction in the basin (Run 3: $\Delta\rho$ = 20 kg.m$^{-3}$; $Q_1$ = 0.489 l.s$^{-1}$, grid solidity $\phi$ = 1/2, Table 2). Initially, the front of the surface outflow is shown to propagate from the channel exit into the basin (Figures 4A–D) before impacting on the upstream face of the grid obstruction, causing the current to thicken locally in the vicinity of the obstruction (Figures 4E–H). The established surface plume propagates through the grid obstruction and is shown to be diminish in thickness away from the locally thickened region immediately downstream of the obstruction (Figures 4I, J). Overall, the presence of the grid obstruction in the basin appears to reduce the occurrence of billows characteristic of interfacial instabilities (e.g. Kelvin-Helmholtz instabilities) in the expanding surface current compared to the unobstructed flow. This obstruction effect on flow instability is analyzed in section 3.2.2.

## 3.2 Quantitative measurements

### 3.2.1 Near-surface density measurements

Figure 5 shows an example of the time series of micro-conductivity probe measurements obtained in the near-surface layer at the channel exit (i.e. probe C1, see Figure 2B) and further downstream into the basin (i.e. probes C2 – C4, see Figure 2B) for run R3 (see Table 2), with different levels of grid obstruction (i.e. solidity $\phi$ = 0, 1/3 and 1/2). The time series surface density excess ($\Delta\rho = \rho_2 - \rho_1$) measurements clearly show the downstream propagation of the surface buoyant jet from the confined channel exit as it expands into the basin (i.e. probes C1 → C4, Figure 5). Specifically, the density measurements at probe C1 (i.e. at the channel exit) show a sharp initial reduction in the density excess $\Delta\rho$ as the mixed head of the surface freshwater outflow arrives at the probe, with a more gradual subsequent reduction in $\Delta\rho$ (with $\Delta\rho \rightarrow 0$) with increasing elapsed time as the body of the quasi-steady surface outflow becomes fully established. For experimental runs with no grid obstruction in place [i.e. Figure 5A, solidity $\phi$ = 0.0], the measured density excess $\Delta\rho$ at probe C2 also shows an initial sharp reduction (at a later time than for probe C1), but then indicates significant fluctuations in $\Delta\rho$ over the remaining time. The density fluctuations measured at C2 probe are shown to reduce in the presence of the grid obstruction with increasing solidity $\phi$ (i.e. solidity $\phi$ = 1/3 and 1/2, Figures 5B, C, respectively). The variability in $\Delta\rho$ appears to be related to the formation of shear-instabilities between the outflowing surface layer and underlying ambient fluid. Initial reductions in the density excess $\Delta\rho$ are also observed further downstream at probes C3 and C4, but the overall reduction in the $\Delta\rho$ values and their temporal variability is shown (Figure 5A) to diminish at locations further downstream into the basin as the surface plume continues to expand laterally and, thus, diminish in thickness.

#### 3.2.1.1 Frontal propagation of expanding surface plume

The downstream propagation of the head of the expanding surface current on exiting the channel can be tracked by analyzing the sequential timings of the initial sharp reduction in density excess $\Delta\rho$ values measured at probes C2 – C4 (see Figure 5), relative to the time of the initial $\Delta\rho$ reduction at probe C1 (i.e. at the end of the channel). Figure 6A shows the dimensional elapsed times $t$ at which the frontal location $x_f$ of the surface plume head reaches the locations of micro-conductivity probes C2, C3 and C4 relative to probe C1 where ($x_f$, $t$) = (0,0). The results indicate that the overall travel time of the plume head is significantly lower for the non-obstructed runs (i.e. run R3, $\phi$ = 0) compared with equivalent runs

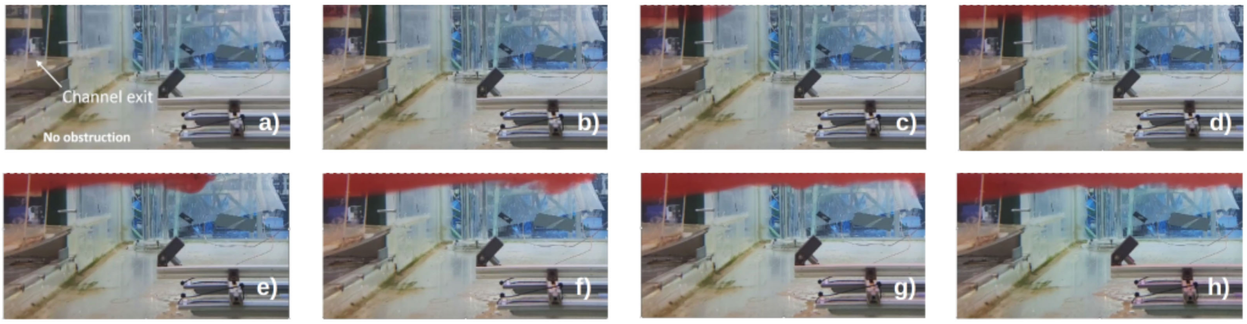

FIGURE 3
Time sequence of dye tracing images showing view from the side of the frontal propagation of the surface gravity current left to right from the exit of the confined channel into the basin and the establishment of a quasi-steady surface flow (Run R5: Δρ = 10 kg.m$^{-3}$; $Q_1$ = 0.244 l.s$^{-1}$, no vertical grid obstruction present) Images shown **(A-H)** are taken at elapsed times t = 0.0 s; 1.33 s; 3.30 s, 5.66 s, 8.41 s; 11.24 s; 14.60 s; 24.12 s, respectively.

FIGURE 4
Time sequence of dye tracing images showing the frontal propagation of the surface gravity current from the exit of the confined channel into the basin and interaction with a vertical grid obstruction (Run R3: $\Delta\rho$ = 20 kg.m$^{-3}$; $Q_1$ = 0.489 l.s$^{-1}$, grid solidity $\phi$ = 1/2). Images shown **(A-J)** are taken at elapsed times $t$ = 0.0 s; 1.87 s; 3.45 s, 4.57 s, 6.23 s; 7.66 s; 9.07 s; 10.81 s; 12.76 s; 14.94 s, respectively. Note: images **(I, J)** show downstream interaction of quasi-steady surface current with grid obstruction.

with the grid obstruction in place (i.e. run R3, $\phi$ = 1/3 and 1/2). It is interesting, however, that the head travel time $t$ does not differ significantly when the grid solidity increases (i.e. run R3, $\phi$ = 1/3 → 1/2) for otherwise identical parametric conditions. By contrast, a reduction in the input volume flux $Q_1$ (i.e. $Q_1$ = 0.489 → 0.244 l.s$^{-1}$, runs R3 → R5, Table 2) for the same grid obstruction solidity (i.e. $\phi$ = 1/3) leads to a corresponding increase in the propagation time $t$ to probe C4. Overall, the gradients of the $x_f : t$ curves suggests that the frontal propagation speed increases from probes C2 → C4 in the unobstructed cases, but slows down on encountering the grid obstructions immediately upstream of probe C2.

Scaling the frontal position $x_f$ versus $t$ by the momentum length scale $l_M$ (see Equation 5), such that $x^\star = x_f / l_M$, and the elapsed time $t$ by the mean surface current velocity $\bar{u}_1$ and length scale $l_M$, such that $t^\star = t \cdot \bar{u}_1 / l_M$, shows that the obstructed frontal propagation collapses relatively well for different input volume fluxes $Q_1$ (i.e. R3 and R5, Table 2) and grid solidities $\phi$ (= 1/3 and 1/2) (see Figure 6B). This figure also shows that the frontal head position tends to slow down after interaction with the grid obstruction, whereas in the non-obstructed runs (i.e. $\phi$ = 0), the propagating head continues to speed up with increasing downstream distance. Comparison between the magnitude of these propagating frontal head velocities and the quasi-steady velocity within the main body of the expanding surface current is discussed in Section 3.2.2.

### 3.2.1.2 Density fluctuations in vicinity of grid

As previously noted, the presence of the grid obstructions [i.e. $\phi$ = 1/3 and 1/2 in Figures 5B, C, respectively] is shown to reduce

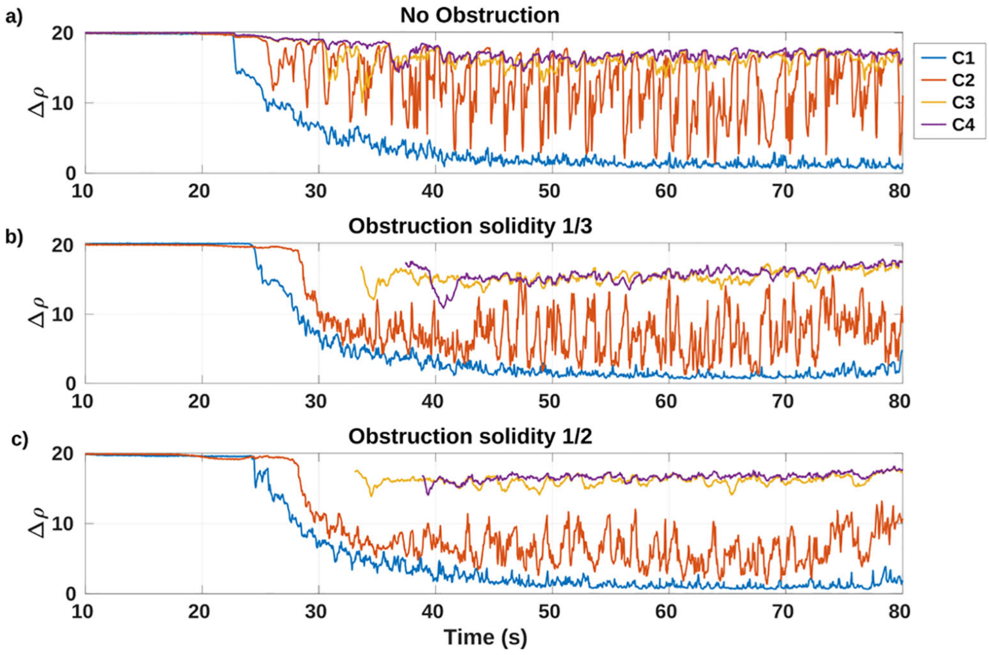

FIGURE 5
Time series of density excess $\Delta\rho = \rho - \rho_1$ measurements obtained during run R3 (see Table 2) with **(A)** no grid obstruction (i.e. solidity $\phi$ = 0.0); and **(B, C)** grid obstruction with solidity $\phi$ = 1/3 & 1/2, respectively.

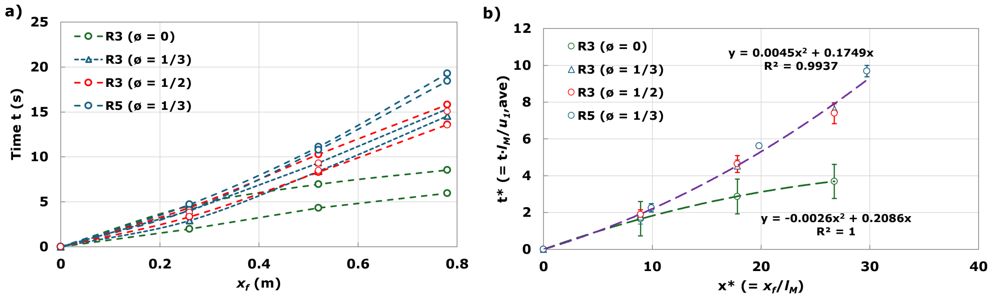

FIGURE 6
**(A)** Temporal evolution of head of the expanding surface plume position $x_f$ measured at probes C2 – C4, relative to probe C1, and **(B)** non-dimensional head position $x^*$ versus normalized time $t^*$ for runs R3 and R5 (see Table 2) with obstruction solidity $\phi$ values as shown.

systematically the degree of density excess $\Delta\rho$ fluctuations observed at probe C2 (i.e. immediately downstream of the grid obstructions) when compared to equivalent runs with no grid obstruction present (i.e. $\Delta\rho$ fluctuations decrease as $\phi = 0 \rightarrow 1/3 \rightarrow 1/2$). By contrast, the $\Delta\rho$ fluctuations measured at probes C1, C3 and C4 appear to be largely unaffected by the presence (or otherwise) of the grid obstructions, indicating that the grids have a relatively localized effect on the density fluctuations within the upper expanding layer. Indeed, it is interesting to compare the density fluctuations $\rho'$ at probe C2, calculated as a variation from the mean surface layer density $\bar{\rho}$ at C2, such that:

$$\rho'_{C2} = \rho_{C2} - \bar{\rho}_{C2} \tag{10}$$

where $\rho_{C2}$ is the instantaneous time series measurements of surface density at probe C2 over the duration of the quasi-steady surface flow period (~40 s). Figures 7A, B show these fluctuations at C2 for runs R3 and R5 (see Table 2), both when the grid obstructions are present and absent. In the unobstructed case (i.e. $\phi = 0$), the strongest density fluctuations (i.e. $\rho'_{C2}$ = -10 → +5 kg.m$^{-3}$, Figures 7A, B) appear to be associated with the generation of large-scale Kelvin-Helmholtz instability at the shear interface between the spreading surface flow and underlying quasi-stationary ambient waters. The manifestations of the instability appear to be suppressed in the presence of a grid obstruction, meaning the density fluctuations $\rho'_{C2}$ also diminish at C2 as the grid solidity increases (i.e. $\rho'_{C2}$ = -5 → +8 kg.m$^{-3}$ for $\phi = 1/3$, Figure 7A; $\rho'_{C2}$ = -5 → +5 kg.m$^{-3}$ and -7 → +2 kg.m$^{-3}$ for $\phi = 1/2$, Figures 7A, B, respectively].

This apparent suppression of the interfacial instability and consequent overturning and mixing in the vicinity of probe C2 is investigated in more detail through determination of the variance distribution of density fluctuations $\rho'_{C2}$ in the frequency domain. Figures 7C, D shows the spectral analysis of the time series of density fluctuations using the Fast Fourier Transform for the unobstructed (i.e. $\phi = 0$) and obstructed (i.e. $\phi$ = 1/3 and 1/2) cases in runs R3 and R5 (see Table 2). At lower frequencies within all spectra, the decaying range of the density fluctuation measurements can be roughly approximated by -5/3 slope, typical of three-dimensional cascading turbulent flow. Larger spectral energy values are also generally associated with the unobstructed flow cases, suggesting a greater degree of shear-induced overturning and mixing compared with the obstructed cases. Furthermore, a reduction in the freshwater volume flux $Q_1$ (i.e. 0.489 → 0.244 l.s$^{-1}$, run R3 → R5) also results in lower energy spectra values, particularly in the obstructed case (i.e. with solidity $\phi = 1/2$, Figure 7D).

The finding that the presence of the grid obstructions reduces the magnitude of density fluctuations and, hence, suppresses interfacial overturning and mixing immediately downstream from the obstruction is somewhat counter-intuitive given grids are often used for turbulence production (Xiang et al., 2015). As a consequence, the overall effect of the grid obstruction in the vertical transfer and mixing of the expanding freshwater surface layer is that it acts as a partial barrier or control on the horizontal surface current propagation, causing a freshwater back-up behind the obstruction that diminishes the formation of interfacial instabilities at C2 (i.e. immediately downstream of the barrier). This suppression of surface layer mixing and the formation of large-scale instabilities is also indicated in the dye visualizations with and without the grid obstruction in place (i.e. comparing Figures 3, 4).

### 3.2.2 Surface layer velocity profiles

Measurements of the velocity structure of the outflowing buoyant surface layer were obtained by UVP probes located at the channel exit (i.e. UVP A, Figure 2B) and downstream of the grid obstruction location between micro-conductivity probes C2 and C3 (i.e. UVP B, Figure 2B). In this context, Figure 8 shows the time-averaged velocity profiles obtained at UVP A and UVP B over the quasi-steady surface flow period for both the unobstructed (i.e. $\phi = 0$) and obstructed (i.e. $\phi$ = 1/3 and 1/2) flow cases. Focusing firstly on the unobstructed cases (Figures 8A, B), an increase in the imposed density excess $\Delta\rho$ (i.e. 0 → 10 → 20 kg.m$^{-3}$, runs R1 → R2 → R3, Table 2) leads to an corresponding increase in the near-surface flow velocity within the gravity current at the channel exit (i.e. $U_1$ = 0.022 → 0.047 → 0.057 m.s$^{-1}$ at UVP A, respectively, Table 2) due to the generation of stronger induced buoyancy-driven flow. It is interesting also to note that the upper layer thickness $h_1$ at the channel exit also reduces with increasing density excess $\Delta\rho$. Measurement comparisons for the UVP A velocity profiles in unobstructed (i.e. $\phi$ = 0, Figure 8A) and

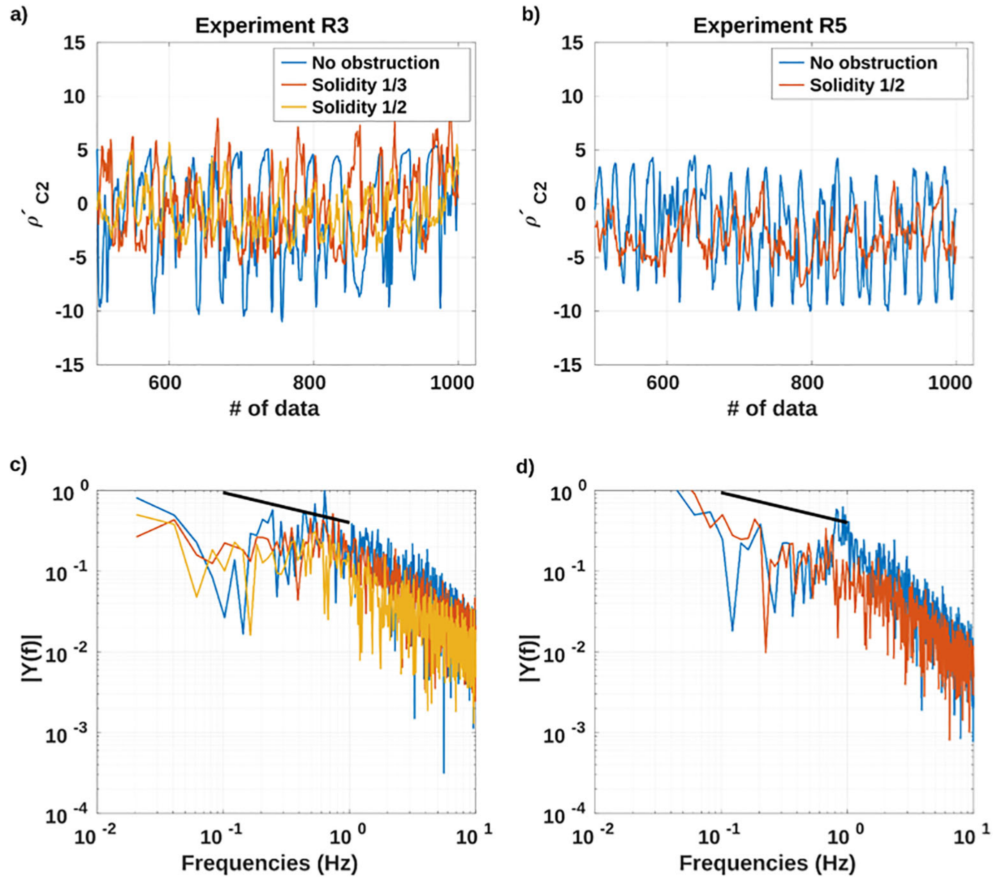

FIGURE 7

**(A, B)** Plots of density fluctuations $\rho'_{C2}$ [Equation 10] for runs R3 and R5 (Table 2) for unobstructed (i.e. $\phi$ = 0) and obstructed (i.e. $\phi$ = 1/3 and 1/2) surface flows at probe C2 during the quasi-steady period. **(C, D)** power spectra of density fluctuation time-series for runs R3 and R5 (Table 2) at probe C2. Note: -5/3 turbulent decay is also shown as solid line.

obstructed (i.e. $\phi$ = 1/3 and 1/2, Figures 8C, E) flow cases do not show any significant differences in either the velocity structure or magnitude within the outflowing surface layer at the channel exit. The lateral expansion of the gravity current into the unobstructed basin (i.e. $\phi$ = 0) is shown to result in a significant reduction in the maximum surface layer velocities, with a loss in the surface layer definition observed in the UVP B profiles (Figure 8B), when compared to the equivalent UVP A profiles (Figure 8A). For the equivalent obstructed flow cases (i.e. $\phi$ = 1/3 and 1/2, Figures 8D, F), the presence of the grid is shown to diminish both the surface layer thickness and maximum velocity at UVP B for runs with $\Delta\rho$ = 10 and 20 kg.m$^{-3}$. It is interesting to note that for runs with a non-buoyant input (i.e. $\Delta\rho$ = 0 kg.m$^{-3}$), the outflowing surface layer lacks any clear definition in the vertical, while the effect of the grid obstruction on reducing the velocity magnitude is most evident when the grid solidity $\phi$ = 1/2 (Figure 8F). Finally, for runs in which the volume flux $Q_1$ is reduced [i.e. $Q_1$ = 0.244 l.s$^{-1}$, runs R4 and R5], the corresponding reduction in the momentum flux $M_1$ (Equation 2) in the upper layer is reflected by a decrease in the maximum near-surface velocities observed at both UVP A and UVP B, as well as a reduction in the surface layer thickness $h_1$ at the channel exit (i.e. at UVP A for $\Delta\rho$ = 20 kg.m$^{-3}$; run R5, Figures 8A, E).

In summary, the presence of the grid obstruction in the basin does not appear to affect significantly either the velocity structure or magnitude in the surface outflow currents generated at the channel exit (i.e. UVP A), for otherwise identical parametric conditions. However, it does affect the velocity structure measured downstream of the grid obstructions (when compared to the equivalent unobstructed flows), whereby the obstructed flow velocity magnitude and surface layer thickness are diminished significantly downstream of the grid obstruction (i.e. at UVP B).

### 3.2.2.1 Shear-induced instabilities and localized effect of obstruction

High velocity gradients generated in the interfacial regions of density stratified flows can contribute to the formation of hydrodynamic shear instabilities that can induce overturning and mixing between the layers. The stability of the interface in density stratified flows can be characterized by the bulk Richardson number $Ri$ (as defined in Equation 7), which compares the relative importance of buoyancy forces and shear forces in a density stratified flow. In the present study, values of $Ri$ are calculated at UVP B using the velocity profile measurements with the corresponding density excess $\Delta\rho$ measurements obtained at probe

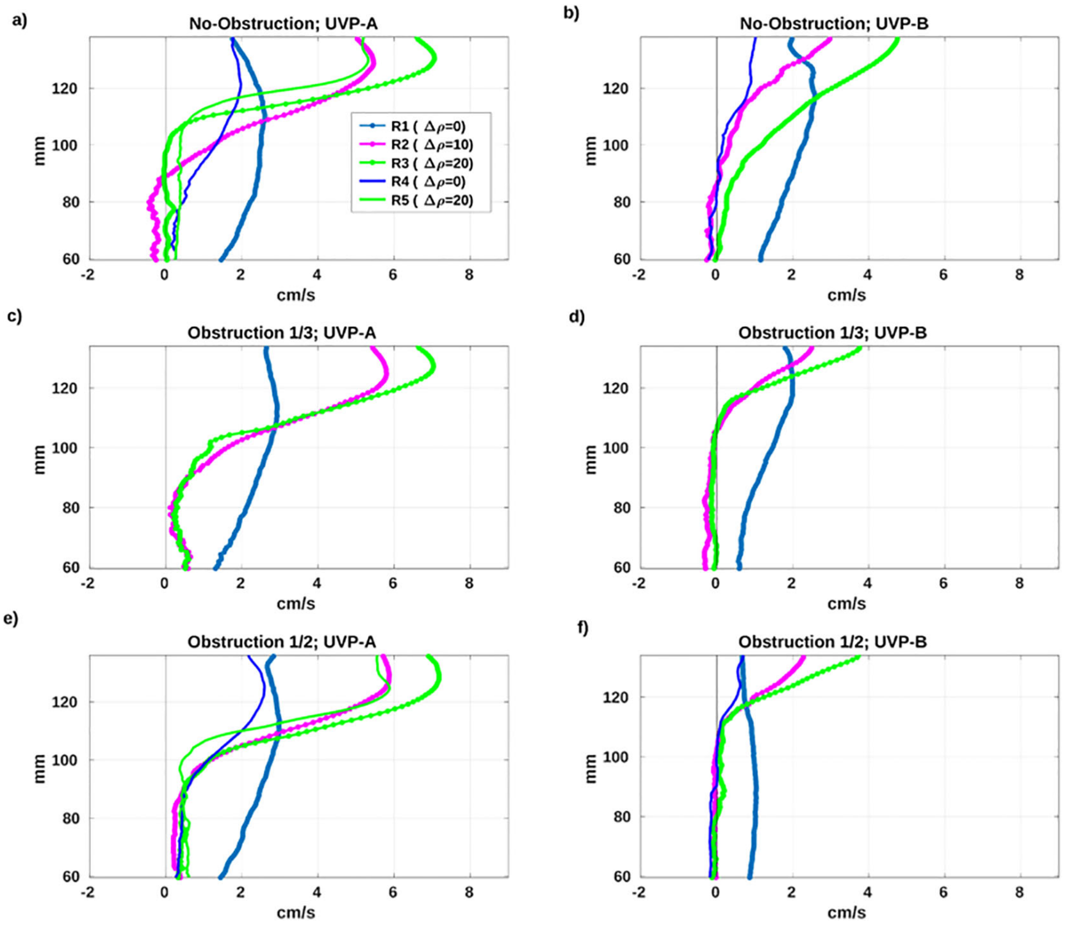

FIGURE 8
Vertical profiles of the time-averaged, centreline along-channel velocity $U$ component obtained for the runs shown at UVP A [i.e. at the channel exit: **(A, C, E)**] and UVP B (i.e. in the basin: **(B, D, F)**]. Corresponding velocity profiles are obtained for the unobstructed flow cases [i.e. with $\phi$ = 0; **(A, B)**] and the obstructed flow cases [i.e. with $\phi$ = 1/3; **(C, D)** and $\phi$ = 1/2; **(E, F)**].

C2 during the quasi-steady state surface outflow conditions. In this regard, Equation 7 can be rewritten as follows:

$$Ri = \frac{g'\delta}{\Delta u^2} \approx \frac{g\overline{\Delta\rho}\delta}{\rho_1 (U_{1,max})^2} \tag{11}$$

where $\overline{\Delta\rho}$ is the average density excess value at a specific location during the quasi-steady surface outflow and $U_{1,max}$ is the maximum time-averaged velocity in the outflowing surface layer (note: this implicitly assumes the time-averaged lower layer velocity $U_2$ = 0). When the layer thickness $\delta$ (Equation 8) becomes small, the bulk Richardson number approaches the gradient Richardson number $Ri_g$, for which the critical value for (linear) instability is around $Ri_g \approx 0.25$, below which shear forces dominate, indicative of an unstable flow (i.e. shear instabilities generated at the interface). These stability conditions are further investigated both at the channel exit (via UVP A, probe C1) and immediately downstream of the obstruction location in the basin (via UVP B, probe C2) in Table 3.

It is interesting to note that the calculated bulk Richardson numbers $Ri$ are considerably lower at the channel exit (i.e. UVP A) than at the location further downstream into the basin (i.e. UVP B). As anticipated, the presence (or otherwise) of the grid obstruction in the basin does not appear to affect the $Ri$ values at the channel exit (ranging from $Ri$ = 0.63 – 0.78 for run R2 and $Ri$ = 0.53 – 0.75 for run R3). The interfacial stability analysis using UVP A and C1 measurements is inconclusive in respect of the impact of the grid obstruction on bulk Richardson number $Ri$ values at the channel exit, mainly as this is located well upstream of the obstruction. These $Ri$ values are, however, larger than the critical value of the gradient Richardson number $Ri_g > \sim 0.25$ for interfacial layer linear stability, although it is noted that this theoretical stability criterion only applies to local gradients (rather than density and velocity differences measured across the interface layer for the bulk Richardson number $Ri$). When considering again the dye images of the surface outflow from the channel (see Figures 3, 4), this indicates that K-H interfacial instabilities develop well into the basin, once the surface plume has thinned as a result of the loss of channel confinement (see Figure 9A). By contrast, in the presence of the downstream grid obstruction (Figure 9B), these K-H instabilities do not seem to occur, even though the surface current still thins on exiting the channel confinement, before thickening again at the upstream face of the grid obstruction.

At the downstream location (UVP B), the equivalent bulk Richardson numbers $Ri$ are considerably larger (ranging from

FIGURE 9
Dye images showing **(A)** formation of K-H instabilities in unobstructed basin (run 3, $\phi$ = 0, Table 2) and **(B, C)** suppression of K-H instabilities in obstructed basin (run 3, $\phi$ = 1/2, Table 2).

$Ri$ = 1.21 – 1.75 for run R2 and 1.61 – 2.07 for run R3) than at UVP A, whether or not a grid obstruction is present. However, unlike at UVP A, a general trend is shown at UVP B that the bulk Richardson number $Ri$ increases (i.e. the interface becomes more stable) for increasing grid solidity $\phi$ and density excess $\Delta\rho$. This is largely due to the increase in local $g'$ and $\delta$ values in run R3 compared to run R2 (see Table 3), while $U_{1,max}$ values are also larger for run R3 compared to run R2, but reduce with increasing grid solidity $\phi$ in both cases. Similarly, the shear mixing layer thickness $\delta$ at UVP B is also shown to reduce as the grid solidity $\phi$ increases (although only marginally between $\phi$ = 1/3 and 1/2).

The larger $Ri$ values obtained when the grid obstruction increases are also consistent with the observed reduction in density fluctuations $\rho'_{C2}$ (i.e. measured at probe C2, see Figure 7), which are typically reduced downstream of the obstruction as the grid solidity $\phi$ increases, as noted in section 3.2.1. Overall, these larger $Ri$ values indicate more favorable conditions for the development of a stably-stratified surface outflow, particularly downstream of the grid obstruction, although this does not preclude the formation of some instabilities at the interface. In addition, the dye images highlight the local deepening of the interface (Figures 9B, C) for the obstructed surface outflow cases, both immediately upstream and downstream of the grid obstruction. This indicates that vertical motions occur in the upper outflowing layer, both upstream and downstream of the obstruction, due to the partial blockage effect. The limited spatial extent of this interface deepening is confirmed by the velocity profile measurements obtained at UVP B (Figures 8D, F), which show the outflowing surface layer thickness downstream of the grid obstruction to be actually reduced when compared to the equivalent layer thickness at UVP B for the unobstructed surface outflows (Figure 8B).

In summary, the presence of the grid obstruction appears to suppress interfacial instabilities and mixing in the downstream flow region, whilst providing more favorable conditions for the formation of stably-stratified surface outflows. This is slightly counter-intuitive and contrary to the expectation that grid obstructions would induce additional turbulence and mixing within the outflowing surface layer (Kurian and Fransson, 2009; Xiang et al., 2015). The exception to this is in close vicinity to the grid obstruction, where vertical motions induce a local thickening of the surface layer. The implications of these findings for surface freshwater plume interactions with aquaculture infrastructure sited in sheltered coastal regions are discussed below.

## 3.3 Comparison with surface outflow in Fangar Bay (Ebro Delta)

Fangar Bay, within the Ebro Delta (NW Mediterranean Sea), provides a good example with which to upscale the laboratory experimental results to a real coastal lagoon containing extensive aquaculture infrastructure. The bay is a micro-tidal estuary with a length of approximately 6 km, a maximum width of 2 km, and an average depth of about 2 m. Field measurements presented in Balsells F-Pedrera et al. (2020) illustrate a quasi-permanent stratification in the water column, even with the presence of aquaculture-related obstructions (in this case, predominantly oyster and mussel rafts), as is shown schematically in Figure 10. In this location, freshwater inflows from terrestrial channels discharging into the bay are of the order of 3 m$^3$.s$^{-1}$, with the mussel rafts located at about 350 m offshore from the freshwater discharge point. Lateral expansion of the surface plume generated by the discharge from a terrestrial channel is detected from a Sentinel-2 image of July 2022 (Figure 10C). In this regard, it is possible to estimate the bulk Richardson number for the stratified flow conditions in Fangar Bay from field data measurements. Firstly, deeper waters in the bay were measured as having a salinity up to 37 PSU and an average water temperature of 26°C (equivalent to an ambient density $\rho_a$ = 1024.5 kg.m$^{-3}$) (Balsells F-Pedrera et al., 2021). The equivalent reduced gravity $g'$ for a terrestrial freshwater outflow with density $\rho_1$ = 1000 kg.m$^{-3}$ is calculated as $g' = g(\Delta\rho/\rho_1)$ = 0.240 m.s$^{-2}$. The interfacial thickness $\delta$ was estimated as 0.04 m and the mean velocity in the upper layer $\bar{u}_1$ = 0.1 m.s$^{-1}$, according to Lagrangian buoy experiments undertaken in June 2022 (see trajectory in Figure 10B). For these conditions, the estimated bulk Richardson number $Ri = g'\delta/\bar{u}_1^2$ = 0.96, confirming the stable density stratification observed in the water vertical column (see salinity profile shown in Figure 10B) within the bay and in good agreement with the $Ri$ values in the laboratory experiments (i.e. between the calculated $Ri$ values at UVP A and B, Table 3). The jet/plume transition length scale (Equation 5) for this real case is estimated as $l_M$ = 0.478 m, which is consistent with buoyancy-dominated surface plume conditions being generated prior to the interaction the mussel rafts, as similarly observed in the experimental runs upstream of the grid obstructions (see equivalent $l_M$ estimates in Table 2). Furthermore, the equivalent Reynolds number of the surface outflow into the bay, where $Re = \bar{u}_1 h_1/\nu \approx$ 10,000 (for an estimated surface layer thickness $h_1$ = 0.1 m), is also similar to the mildly turbulent flow

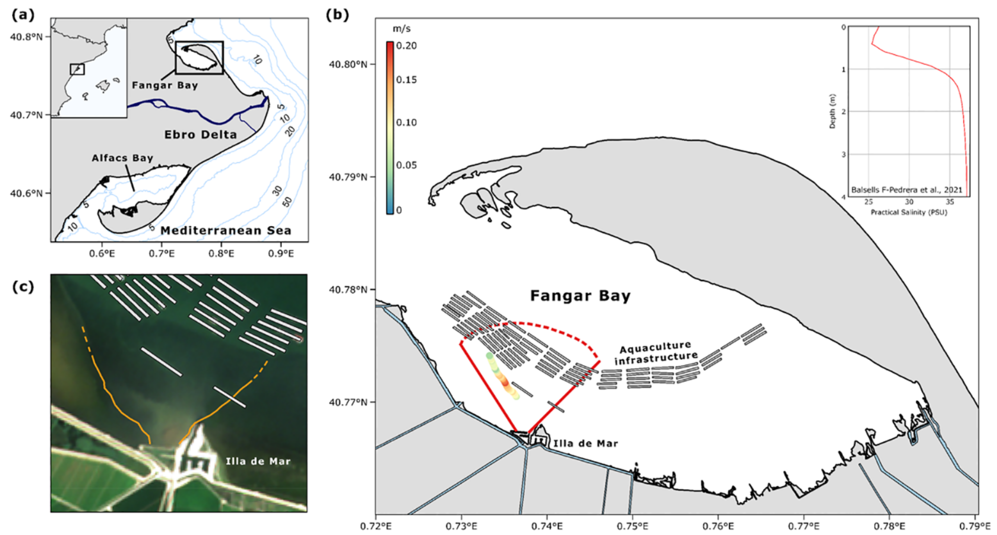

FIGURE 10

The case of Fangar Bay as example of buoyant plume interaction with aquaculture rafts in a micro-tidal environments. **(A)** Location map of Fangar Bay in NW Mediterranean Sea. **(B)** Fangar Bay map with Lagrangian buoy experiment undertaken on July 2022 (colorbar indicates buoy velocity) and salinity profile from Balsells F-Pedrera et al. (2021). **(C)** Sentinel-2 image from 26th July 2022 with the discharge plume delineated from Illa de Mar terrestrial discharge channel.

conditions in the laboratory experiments. The similarity of the *Ri* and *Re* values between the laboratory and field conditions suggest a relatively straightforward analysis of stratification using vertical profiles of CTD field data, which revealed persistent, stably-stratified conditions in the bay even in the presence of multiple mussel and oyster rafts (Balsells F-Pedrera et al., 2020; 2021). These field results are thus consistent with the overall conclusions of the laboratory study, in that the aquaculture raft obstructions have a marginal overall effect on the expanding surface plumes (and their eventual mixing in the water column), but have more concentrated localized effects in the near vicinity of the rafts.

## 4 Discussion

The experimental results have demonstrated that the presence of a vertical grid obstruction has a partial blockage effect on the outflowing surface flow, leading to a general reduction in the time-averaged velocity and layer thickness of the expanding surface plume downstream of the obstruction, at least for the range of parametric conditions evaluated in the experiments. The presence of the obstruction is also shown to reduce significantly the magnitude of time-varying fluctuations in the density excess $\Delta\rho$ immediately downstream of the obstruction, suggesting that the large-scale vortical flow structures (i.e. evidence of K-H instability) generated from the surface flow expansion at the channel exit into the unconfined basin are diminished by interaction with the grid obstruction. Consequently, the presence of similar obstructions (e.g. aquaculture infrastructure) in sheltered coastal domains may also have a considerable influence on the stratification, turbulent mixing processes, and transfer of substances in the vertical direction in the vicinity of the obstructions, but would be expected to have more limited effect on the wider dispersion of the surface plume. As suggested previously, the localized impact of the surface plume near the vicinity of the obstruction is contrary to the initial assumption that the grid obstructions would generate additional turbulence and, hence, promote mixing and the breakdown of stable stratification within the expanding surface flow. This mixing has been observed and measured previously in other studies of grid-induced turbulence within stratified flows (e.g. Xiang et al., 2015) and open channel flow interactions with aquaculture net panels (e.g. Shao et al., 2021; Zeng et al., 2022). However, the contrary findings in the current study are most likely to be associated with the relatively low Reynolds numbers for the expanding, buoyancy-driven, surface plumes, which are insufficient to induce additional mixing on encountering the grid obstructions. Conducting physical experiments at higher Reynolds numbers (i.e. through significantly increasing the surface volume flux $Q_1$) would most likely result in greater disruption of the stable stratification on encountering the grid obstructions. However, achieving higher Reynolds number surface flows would lie outside the typical environmental flow conditions encountered in semi-enclosed lagoons containing aquaculture infrastructure [e.g. as demonstrated in Fangar Bay, where estimated Reynolds numbers $Re = O(10^4)$].

It is also interesting to consider, for the surface buoyant flow through the vertical grid obstructions, the equivalent Reynolds numbers scaled on the vertical grid bar $d$ and slot $s$ widths [i.e. where $d = 0.005$ m is the fixed length scale of the grid bars, with $s = 0.01$ m (for $\phi = 1/3$) and 0.005 m (for $\phi = 1/2$), Figure 2C], which can be defined as follows:

$$Re_d = \frac{\bar{u}_1 d}{\nu}; \quad Re_s = \frac{\bar{u}_1 s}{\nu} \tag{12}$$

where $\bar{u}_1$ is the mean surface layer-averaged velocity measured upstream of the grid obstruction and ν is the kinematic viscosity of the water. In runs R2, R3 and R5, the mean surface layer velocities $\bar{u}_1$ = 0.0468 m.s$^{-1}$, 0.0572 m.s$^{-1}$ and 0.0511 m.s$^{-1}$, respectively (i.e. measured at UVP A, Table 2), resulting in corresponding $Re_d$ values of 234, 286 and 256 ($\equiv Re_s$ for $\phi = 1/2$), and $Re_s$ = 468, 572 and 512, respectively (for $\phi = 1/3$). These values correspond to the 3D wake-transition (i.e. $190 < Re_d < 260$) and transitional turbulent regimes ($Re_d > 260$), based on the vortex shedding regimes past cylinders in homogeneous flows (Williamson, 1996). Further laboratory simulations with larger values of $Re_d$ may induce greater vertical mixing further away from the obstruction in a similar vein to offshore wind farm impacts on stratified shelf seas (e.g. Cazenave et al., 2016).

The lack of laboratory (or indeed field) measurements in the near-vicinity of the grid obstructions means that the exact nature of the flow structure through the grid obstruction, and vortex field generated immediately downstream, is difficult to resolve. However, a number of previous experimental and numerical studies have considered the streamwise velocity and vortex fields generated by a side-by-side pair of square bluff bodies or circular cylinders under a similar range of low Reynolds numbers to the current studies (e.g. Davis et al., 1984; Sanyal and Dhiman, 2017; 2018). The numerical study of Sanyal and Dhiman (2018) indicated that when $Re_d = 300$ and $s/d = 1.0$, the streamwise velocity through the gap between the two square bluff bodies increased to 1.33 times the maximum streamwise velocity $U_{max}$ upstream of the bluff bodies, while the velocity recovery at $x/d = 4.6$ downstream of the bodies was about 0.5 $U_{max}$. For the same $Re_d = 300$ and $s/d = 2.0$, the streamwise velocity through the gap remained at 1.33 $U_{max}$ with the velocity recovery at $x/d = 4.6$ equal to about $0.8 \cdot U_{max}$.

Within the current laboratory experiments, the ratio of the maximum time-average surface layer velocities $U_{1,max}$ at UVP B and UVP A is shown to range between 0.55 – 0.66 for the unobstructed cases (i.e. $s/d = \infty$), whereas for the grid obstructions with solidity $\phi = 1/3$ and 1/2 (i.e. $s/d = 2.0$ and 1.0, respectively), the corresponding maximum velocity ratio ranges between 0.43 – 0.54 and 0.39 – 0.51, respectively. It is noted that the position of the UVP B velocity profiles is approximately $x' = 0.25$ m downstream of the grid obstructions (i.e. $x'/d = 50$, where $x' = 0$ at the grid obstruction). As there is very little variation observed in the $U_{1,max}$ values measured at UVP A for either unobstructed or obstructed flows (Figure 8), the measurements at UVP B can be used to assess the velocity recovery due to the presence of the grid obstructions. This can be estimated directly from the ratio of $U_{1,max}$ values at UVP B for the obstructed and unobstructed flows, ranging from 0.81 – 0.83 for grid solidity $\phi$ = 1/3 (i.e. $s/d = 2.0$) and 0.77 – 0.79 for grid solidity $\phi$ = 1/2 (i.e. $s/d$ = 1.0). This shows that the grid obstructed surface flows do not fully recover their surface velocity (with respect to the unobstructed surface flow) even after a significant downstream distance (i.e. $x'/d$ = 50). In some respects, this finding is similar to previous experiments results for open channel flow interactions with aquaculture cage net panels (e.g. Shao et al., 2021; Zeng et al., 2022), where the full recovery of the incoming flow velocities does not take place for a considerable distance $x/M > 10$ downstream of the net panel (where $M$ represents the net mesh dimension). The current experimental configuration is, however, for more complex than these confined flow-net panel interactions, due in part to the three-dimensional nature of the spreading surface buoyant plume on exiting the confined channel (i.e. contributing to the along-channel reduction in the surface layer velocity as a result of this lateral expansion).

Other experimental and numerical efforts have explored the impact of aquaculture infrastructure (including suspended bivalves) on the flow and wave dynamics, with clear effects demonstrated on both increased drag coefficients and wave attenuation (e.g. Fredriksson et al., 2010; Gaurier et al., 2011; Landmann et al., 2021). These studies do not, however, address the potential impacts of buoyant and non-buoyant discharges. The observed feedback between the grid obstructions and the buoyant plume propagation suggest the potential for a localized vertical transfer of substances at the barrier (and, hence, an expected increase in the vertical distribution of nutrients in the vicinity of the aquaculture, with a potentially positive impact on the productivity of shellfish farms). However, these locally-induced vertical motions and downward interfacial displacement in the vicinity of the obstructions also suggests that the grid-induced turbulence generated by aquaculture infrastructure within sheltered micro-tidal coastal embayments is unlikely to induce wider mixing and erosion of the stable pycnoline in the downstream water column (e.g. within Fangar Bay). Indeed, the observed reductions in the surface plume velocities downstream of the grid obstructions are aligned with the experiments findings of Gaurier et al. (2011), who found numerically that oyster farms induce energy dissipation, resulting in a reduction in the mean flow velocities in a homogeneous waterbody. Furthermore, Gaurier et al. (2011) found wake decelerations to be of the order of 20%, which is entirely consistent with the comparison of obstructed and unobstructed flow cases in UVP B, as detailed above.

Finally, the idealized grid obstruction design tested in our experiments may differ significantly from more realistic fish cages and shellfish rafts. In this case, we designed a simple geometry (i.e. solid vertical bars and vertical gaps) that provided an obstruction with straightforward solidity $\phi$ and $s/d$ ratio. In this regard, experimental analysis of the impact of freshwater discharges with more realistic obstruction geometries (i.e. real mussel ropes or surrogates), similar to that presented by Landmann et al. (2021) or Gaurier et al. (2011) for homogeneous waterbodies, may provide more realistic results and increase the understanding of the local flow fields in the vicinity of shellfish dropper lines, oyster cages, or other common aquaculture infrastructure. Future experimental research could also utilize more sophisticated flow visualization tools and measurement techniques (e.g. PIV, PLIF), as well as advanced Computational Fluid Dynamics (CFD) models to gain more detailed insight into the local impacts of the aquaculture-derived obstructions on the structural evolution of the surface buoyant currents and, in particular, the specific vertical transport mechanisms near the obstruction and turbulent wake field downstream of the obstructions.

## 5 Conclusions

Grid obstructions, including infrastructures and rafts used in shellfish and mussel aquaculture, significantly affect incident surface buoyant jets. The experiments conducted in this study illustrate the influence of grid obstructions on the velocity of frontal propagation, while demonstrating a minor effect on the expansion of surface buoyant jets downstream of the obstruction. Reduction of measured density fluctuations downstream the obstruction suggest a suppression of the instabilities generated at the interface by presence of grid obstruction. This is further corroborated by flow visualization using dye, which compares the obstructed and unobstructed experiments. The increase in bulk Richardson number for grid obstruction experiments indicates a more stable stratification in steady-state buoyant outflows, resulting in reduced interfacial instabilities. This is consistent with observed local deepening of the fresh-salt water interface near the obstruction; which local turbulent mixing and vertical transfer of substances may be relevant but have relatively minimal impact in the final dispersion of the plume. This finding is unexpected and contradicts the expectation that grid obstructions would induce additional turbulence and mixing within the outflowing surface layers. This discrepancy can be attributed to the relatively low Reynolds number tested, indicating mildly turbulent flow conditions that are consistent with real conditions observed in the literature for micro-tidal environments.

## Data availability statement

The raw data supporting the conclusions of this article will be made available by the authors, without undue reservation.

## Author contributions

MG: Conceptualization, Data curation, Formal analysis, Funding acquisition, Investigation, Methodology, Project administration, Resources, Software, Supervision, Validation, Visualization, Writing – original draft, Writing – review & editing. AC: Writing – original draft, Writing – review & editing. RP: Writing – original draft, Writing – review & editing. PD: Writing – original draft, Writing – review & editing.

## Funding

The author(s) declare financial support was received for the research, authorship, and/or publication of this article. This work is supported by ECOBAYS funded by the Spanish Agency of Investigation (PID2020-115924RB-I00), Spanish Ministry of Science and Innovation.

## Acknowledgments

The first author, MG, acknowledges the Salvador Madariaga program (PRX21/00589–2021) from the Spanish Ministry of Education that supports this collaboration. The authors also thank the technical support team at the School of Science and Engineering (Civil Engineering), University of Dundee, for their invaluable help in setting up the experiments that were carried out in this study.

## Conflict of interest

The authors declare that the research was conducted in the absence of any commercial or financial relationships that could be construed as a potential conflict of interest.

## Publisher's note

## References

Balsells F-Pedrera, M., Grifoll, M., Espino, M., Cerralbo, P., and Sanchez-Arcilla, A. (2020). Wind-driven hydrodynamics in the shallow, micro-tidal estuary at the Fangar Bay (Ebro Delta, NW Mediterranean Sea). *Appl. Sci.* 10, 6952. doi: 10.3390/app10196952

Balsells F-Pedrera, M., Grifoll, M., Fernandez-Tejedor, M., and Espino, M. (2021). Short-term response of chlorophyll a concentration due to intense wind and freshwater peak episodes in estuaries: the case of Fangar Bay (Ebro Delta). *Water* 13, 701. doi: 10.3390/w13050701

Bonamano, S., Piazzolla, D., Scanu, S., Piermattei, V., and Marcelli, M. (2021). Trace-metal distribution and ecological risk assessment in sediments of a sheltered coastal area (Gulf of Gaeta, central-eastern Tyrrhenian Sea, Italy) in relation to hydrodynamic conditions. *Mediterr. Mar. Sci.* 22, 372–384. doi: 10.12681/mms.24996

Carminati, M., and Luzzatto-Fegiz, P. (2017). Conduino: Affordable and high-resolution multichannel water conductivity sensor using micro USB connectors. *Sensors Actuators B: Chem.* 251, 1034–1041. doi: 10.1016/j.snb.2017.05.184

Cazenave, P. W., Torres, R., and Allen, J. I. (2016). Unstructured grid modelling of offshore wind farm impacts on seasonally stratified shelf seas. *Prog. Oceanography* 145, 25–41. doi: 10.1016/j.pocean.2016.04.004

Cerralbo, P., Balsells F-Pedrera, M. F., Mestres, M., Fernandez, M., Espino, M., Grifoll, M., et al. (2019). Use of a hydrodynamic model for the management of water renovation in a coastal system. *Ocean Sci.* 15, 215–226. doi: 10.5194/os-15-215-2019

Davis, R. W., Moore, E. F., and Purtell, L. P. (1984). A numerical-experimental study of confined flow around rectangular cylinders. *Phys. Fluids* 27, 46–59. doi: 10.1063/1.864486

De Falco, M. C., Adduce, C., Cuthbertson, A., Negretti, M. E., Laanearu, J., Malcangio, D., et al. (2021). Experimental study of uni-and bi-directional exchange flows in a large-scale rotating trapezoidal channel. *Phys. Fluids* 33, 036602. doi: 10.1063/5.0039251

Duma, D., Erpicum, S., Archambeau, P., Pirotton, M., and Dewals, B. (2014). "Velocity and turbulence measurements for assessing the stability of riverbeds: a comparison between UVP and ADVP," in *Proceedings of the 11th International Conference on Hydroscience & Engineering ICHE*, 539–544.

Eggenhuisen, J. T., Tilston, M. C., de Leeuw, J., Pohl, F., and Cartigny, M. J. B. (2020). Turbulent diffusion modelling of sediment in turbidity currents: An experimental validation of the Rouse approach. *Depositional Rec.* 6, 203–216. doi: 10.1002/dep2.86

Erena, M., Domínguez, J. A., Aguado-Giménez, F., Soria, J., and García-Galiano, S. (2019). Monitoring coastal lagoon water quality through remote sensing: The Mar Menor as a case study. *Water (Switzerland)* 11, 1–19. doi: 10.3390/w11071468

Fischer, H. B., List, E. J., Koh, R. C. Y., Imberger, J., and Brooks, N. H. (1979). *Mixing in inland and coastal waters* (New York: Academic).

Fredriksson, D. W., Steppe, C. N., Wallendorf, L., Sweeney, S., and Kriebel, D. (2010). Biological and hydrodynamic design considerations for vertically oriented oyster grow out structures. *Aquacultural Eng.* 42, 57–69. doi: 10.1016/j.aquaeng.2009.11.002

García-Altares, M., Casanova, A., Fernández-Tejedor, M., Diogène, J., and De La Iglesia, P. (2016). Bloom of Dinophysis spp. dominated by D. sacculus and its related diarrhetic shellfish poisoning (DSP) outbreak in Alfacs Bay (Catalonia, NW Mediterranean Sea): Identification of DSP toxins in phytoplankton, shellfish and passive samplers. *Regional Stud. Mar. Sci.* 6, 19–28. doi: 10.1016/j.rsma.2016.03.009

Gaurier, B., Germain, G., Kervella, Y., Davourie, J., Cayocca, F., and Lesueur, P. (2011). Experimental and numerical characterization of an oyster farm impact on the flow. *Eur. J. Mechanics B/Fluids* 30, 513–525. doi: 10.1016/j.euromechflu.2011.05.001

González-Ávalos, R., Martínez-Estévez, I., Domínguez, J. M., Gironella, X., Crespo, A. J., and Altomare, C. (2024). Numerical simulation of a flexible net in currents with the smoothed particle hydrodynamics method. *Ocean Eng.* 300, 117102. doi: 10.1016/j.oceaneng.2024.117102

Gray, T. E., Alexander, J., and Leeder, M. R. (2006). Longitudinal flow evolution and turbulence structure of dynamically similar, sustained, saline density and turbidity currents. *J. Geophysical Research: Oceans* 111, 1–14. doi: 10.1029/2005JC003089

Huguet, J.-R., Brenon, I., and Coulombier, T. (2020). Influence of floating structures on tide- and wind-driven hydrodynamics of a highly populated marina. *J. Waterway Port Coastal Ocean Eng.* 146, 1–12. doi: 10.1061/(asce)ww.1943-5460.0000549

Jirka, G. H., Doneker, R. L., and Hinton, S. W. (1996). *User's manual for CORMIX: A hydrodynamic mixing zone model and decision support system for pollutant discharges into surface waters* (US Environmental Protection Agency, Office of Science and Technology).

Kurian, T., and Fransson, J. H. (2009). Grid-generated turbulence revisited. *Fluid dynamics Res.* 41, 021403. doi: 10.1088/0169-5983/41/2/021403

Landmann, J., Fröhling, L., Gieschen, R., Buck, B. H., Heasman, K., Scott, N., et al. (2021). Drag and inertia coefficients of live and surrogate shellfish dropper lines under steady and oscillatory flow. *Ocean Eng.* 235, 109377. doi: 10.1016/j.oceaneng.2021.109377

León, V. M., Moreno-González, R., García, V., and Campillo, J. A. (2017). Impact of flash flood events on the distribution of organic pollutants in surface sediments from a Mediterranean coastal lagoon (Mar Menor, SE Spain). *Environ. Sci. pollut. Res.* 24, 4284–4300. doi: 10.1007/s11356-015-4628-y

Lin, H., Chen, Z., Hu, J., Cucco, A., Sun, Z., Chen, X., et al. (2019). Impact of cage aquaculture on water exchange in Sansha Bay. *Continental Shelf Res.* 188, 103963. doi: 10.1016/j.csr.2019.103963

Ramón, M., Fernández, M., and Galimany, E. (2007). Development of mussel (Mytilus galloprovincialis) seed from two different origins in a semi-enclosed Mediterranean Bay (N.E. Spain). *Aquaculture* 264, 148–159. doi: 10.1016/j.aquaculture.2006.11.014

Sanyal, A., and Dhiman, A. (2017). Wake interactions in a fluid flow past a pair of side-by-side square cylinders in presence of mixed convection. *Phys. Fluids* 29, 103602. doi: 10.1063/1.5005118

Sanyal, A., and Dhiman, A. (2018). Effect of thermal buoyancy on a fluid flowing past a pair of side-by-side square bluff-bodies in a low-Reynolds number flow regime. *Phys. Fluids* 30, 063603. doi: 10.1063/1.5025652

Shao, D., Huang, L., Wang, R. Q., Gualtieri, C., and Cuthbertson, A. (2021). Flow turbulence characteristics and mass transport in the near-wake region of an aquaculture cage net panel. *Water (Switzerland)* 13, 1–22. doi: 10.3390/w13030294

Umgiesser, G., Ferrarin, C., Cucco, A., De Pascalis, F., Bellafiore, D., Michol, G., et al. (2014). Comparative hydrodynamics of 10 Mediterranean lagoons by means of numerical modeling. *J. Geophysical Research: Oceans* 119, 3868–3882. doi: 10.1002/2013JC009512

Wilkin, J., Cuthbertson, A., Dawson, S., Stow, D., Stephen, K., Nicholson, U., et al. (2023). The response of high density turbidity currents and their deposits to an abrupt channel termination at a slope break: Implications for channel–lobe transition zones. *Sedimentology* 70, 1164–1194. doi: 10.1111/sed.13073

Williamson, C. H. K. (1996). Three-dimensional wake transition. *Journal of Fluid Mechanics.* 7328, 345–407.

Xiang, X., Madison, T. J., Sellappan, P., and Spedding, G. R. (2015). The turbulent wake of a towed grid in a stratified fluid. *J. Fluid Mechanics* 775, 149–177. doi: 10.1017/jfm.2015.299

Yang, X., Zeng, X., Gualtieri, C., Cuthbertson, A., Wang, R. Q., and Shao, D. (2022). Numerical simulation of scalar mixing and transport through a fishing net panel. *J. Mar. Sci. Eng.* 10, 1511. doi: 10.3390/jmse10101511

Zayed, M., El Molla, A., and Sallah, M. (2018). An experimental study on angled trash screen in open channels. *Alexandria Eng. J.* 57, 3067–3074. doi: 10.1016/j.aej.2018.05.005

Zeng, X., Gualtieri, C., Cuthbertson, A., and Shao, D. (2022). Experimental study of flow and mass transport in the near-wake region of a rigid planar metal net panel. *Aquacultural Eng.* 98, 102267. doi: 10.1016/j.aquaeng.2022.102267

Zhu, D. Z., and Lawrence, G. A. (2001). Holmboe's instability in exchange flows. *J. Fluid Mechanics* 429, 391–409. doi: 10.1017/S002211200000286X